Stability Diagram of Layer-polarized Quantum Hall States in Twisted Trilayer Graphene.

Konstantin Davydov[1†], Daochen Long[1], Jack A. Tavakley[1], Kenji Watanabe[2], Takashi Taniguchi[3], Ke Wang[1*].

AUTHOR ADDRESS

[1]School of Physics and Astronomy, University of Minnesota, Minneapolis, Minnesota 55455, USA

[2]Research Center for Electronic and Optical Materials, National Institute for Materials Science, 1-1 Namiki, Tsukuba 305-0044, Japan

[3]Research Center for Materials Nanoarchitectonics, National Institute for Materials Science, 1-1 Namiki, Tsukuba 305-0044, Japan

Corresponding author: *kewang@umn.edu.

KEYWORDS twisted trilayer graphene, layer-polarized quantum Hall states, stability diagram, Chern number, Chern transitions.

ABSTRACT: In the twisted trilayer graphene (tTLG) platform, the rich beating patterns between the three graphene layers give rise to a plethora of new length scales and reconstructed electronic bands arising from the emergent moiré and moiré-of-moiré superlattices. The co-existing lattices and superlattices interact and compete with each other to determine the overall transport properties of tTLG, the hierarchy of which can be electrostatically controlled by tuning the out-of-plane charge distribution or layer polarization. In this work, we measure the stability diagram of layer-polarized quantum Hall states in tTLG by systematically mapping out layer-specific Chern numbers in each layer, and intra- and interlayer Chern transitions as a function of displacement field D and total carrier density n. In contrast to twisted bilayer systems, the rich interplay between the three atomic layers gives rise to a complex layer-polarized stability diagram with unconventional transport features that evolve rapidly with electric and magnetic fields. The stability diagram quantitatively characterizes the interlayer screening and charge distribution in tTLG with implication of strong inter-atomic-layer Coulomb coupling. Our work provides comprehensive guidance and insights into predicting and controlling layer-polarization and interlayer transitions in tTLG, and for tuning the individual role and interactions of each participating constituent towards novel material properties.

When two pieces of 2D materials are transferred on top of each other with a twist angle, the beating pattern of the two misaligned lattices gives rise to a new lattice periodicity known as moiré superlattice. The reconstructed electronic band can be versatilely tuned by material choices and twist angles combinations, and flat-bands promoting electron correlations have been shown to give rise to a plethora of emergent quantum phenomena such as moiré superconductivity,[1,2] ferromagnetism,[3] correlated insulator states[4–6] and quantum anomalous Hall effect[7–11] in various twisted bilayer systems consisting of homo- or hetero-twisted-interfaces of graphene and transition metal dichalcogenides.[1–14]

The twisted trilayer graphene (tTLG) system has recently attracted great research interest as a new designer material platform.[15–20] The rich interplay between the two co-existing moiré superlattices can lead to distinct atomic landscapes and emergent quantum phenomena depending on the twist angle combination. When two twist angles are alternative and equal, the two moiré superlattices are spatially aligned[15,16] to form a single atomically-reinforced moiré superlattice that is more homogenous, promoting enhanced electron correlation and more robust superconductivity with a higher critical temperature.[21] When the two twist angles are different, the atomic reconstruction between the two moiré superlattices gives rise to a higher order superlattice with a plethora of new length scales including quasi-crystalline lattice[18] and moiré-of-moiré (MoM) superlattice, with emergent new quantum phenomena including inter-moiré Hofstadter butterfly,[22] anomalous quantum Hall (QH) effect,[23] correlated insulator states and signatures of superconductivity at extremely low carrier density (~ 10^{10} cm^{-2}).[17]

The hierarchy of each constituting graphene lattice and moiré superlattice can be manipulated with an out-of-plane displacement field D, which selectively promotes/suppresses each constituting layer in interaction and competition, and thus determines the overall transport behavior. A comprehensive map of charge distribution across each graphene layer in tTLG as a function of

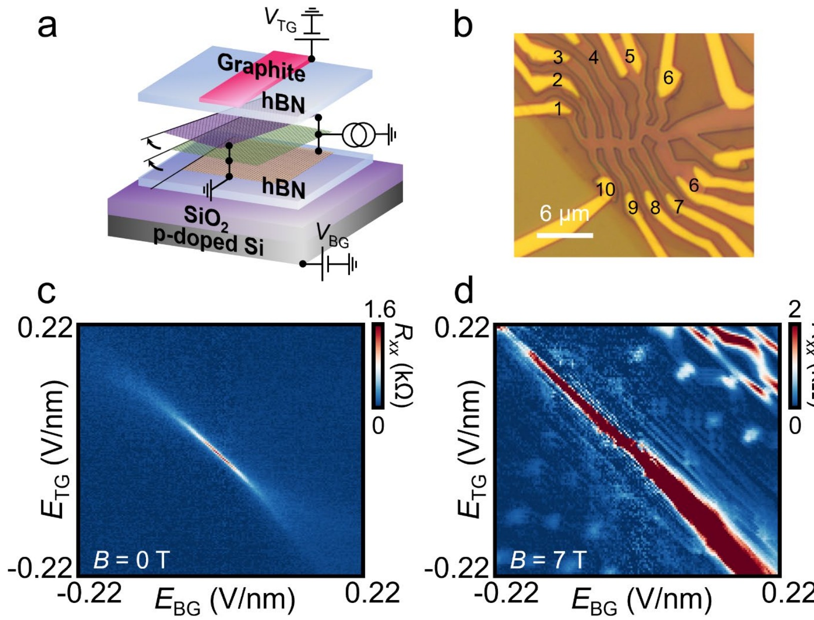

Figure 1. Gate-tunable layer coupling in tTLG. (a) Schematic architecture and measurement configuration of the-dual gated tTLG stack with each monolayer graphene (MLG) layer highlighted by a color (purple: top; green: middle; yellow: bottom). The graphite top (silicon back) gate is at applied voltage $V_{TG}(V_{BG})$. (b) Optical image of the tTLG device used for four-probe electrical transport measurements. The metal contacts to tTLG are labeled with numbers. (c) Four-probe longitudinal resistance R_{xx} as a function of the electric field from the back (E_{BG}) and top gate (E_{TG}) at B = 0 T. The single resistance peak corresponds to the charge neutrality point at n = 0 cm^{-2}. (d) Same as (c) but at B = 7 T. Additional resistance peaks are SdH maxima due to layer-polarized QH states. At $n \neq 0$ cm^{-2}, the resistance peaks position as a function of E_{BG}, E_{TG} characterizes the strength of capacitive coupling between the gates and the respective layer hosting the QH states.

typical experimental parameters (such as top versus bottom gate, or n versus D) would shed important insight in unraveling the microscopic physics mechanism of emergent tTLG quantum phenomena and provide experimental guidance in versatilely tuning and designing the tTLG material properties.

A state-of-the-art electric-only Si/SiGe qubit employs a triple quantum dot (tQD) device architecture, where lateral regions (dots) of confined electrons are tunnel-coupled to each other. A charge stability diagram of tQD[24–27] maps out the charge occupation in each dot as a function of local gate voltages, as well as identifying each intra- and inter-dot charge transitions. Such comprehensive control allows versatile initialization and manipulation of single or two electron states for charge and spin qubit. Similarly, to allow informed systematic electrostatic tuning of the tTLG platform, and to identify and control the role of each underlying microscopic constituents, we study layer-polarized QH states in a twisted trilayer graphene device. We investigate the QH stability diagram of tTLG by mapping out the Chern number in each layer as a function of local gate voltages, as well as identifying each intra- and interlayer Chern transitions.

RESULTS AND DISCUSSION

Layer Capacitive Coupling in Twisted Trilayer Graphene. Three pieces of graphene (top/middle/bottom graphene are marked by purple/green/yellow) are stacked on top of each other with consecutive twist angles (Fig. 1a) of ∼2°, which is subsequently dry etched into Hall bar geometry (see METHODS) with standard 1D edge contacts (Fig. 1b). Similar to a tQD, the twist angle is chosen to be around ∼2° so that each layer in tTLG is tunnel-coupled instead of strongly hybridized. The measured four-probe resistance (Fig. 1c) at B = 0 exhibits high resistance states only at charge neutrality n = 0, without band-insulator states that are otherwise expected at $n = 9\times10^{12}$ cm^{-2} (see Supporting Information-3 for details) when two graphene bands hybridize. Instead, the quantum Hall states[28] become layer-polarized beyond such carrier density and exhibit complex new dependence on carrier density and displacement field under high magnetic field, similar to that of tunnel-coupled tQDs. Figure 1d shows measured longitudinal resistance R_{xx} as a function of the electric field from the top (V_{TG}) and back (V_{BG}) gate voltage $E_{TG} = V_{TG}/d_t$ and $E_{BG} = V_{BG}/d_{bg}$ at B = 7 T, where d_t, d_{bg} are distances from tTLG to the top, back gate respectively. At high carrier density, three sets of layer-polarized Shubnikov-de Haas (SdH) oscillations peaks are clearly visible, each with a distinct slope (of E_{TG} versus E_{BG}) that quantitatively characterizes the gate capacitive coupling ratio of the corresponding graphene layer. The sets of SdH lines with intermediate slope of $|\Delta E_{TG}/\Delta E_{BG}|$ =1 have an equal capacitive coupling of the top and bottom layers, consistent with QH states belonging to the middle graphene layer, whose couplings to the top and bottom gates are equally screened by the top and bottom graphene. The set of the SdH lines with a slanted slope (see Supporting Information-5 for details on determining the slope) of $|\Delta E_{TG}/\Delta E_{BG}|$ <1 (>1) has a capacitive coupling ratio (see Supporting Information-5 for details) of $|C^*_{TG}/C^*_{BG}|$ = 16 (=2.2), consistent with QH states belonging to the top (bottom) graphene layer that has a stronger and unscreened coupling to the top (back) gate, and a weaker and screened coupling to the back (top) gate due to the presence of the middle and bottom (top) graphene layer. From the slopes of these slanted SdH peaks, the effective electric field after screening from two consecutive adjacent graphene layers in electric field is reduced to ~33% (~43%) of its original unscreened value. The slight difference in screening strength by the bottom (top) graphene layers can be attributed to realistic variation in atomic landscape and electronic reconstruction at the bottom (top) moiré interface.

Stability Diagram of Balanced Layer-Polarized Quantum Hall States. Figure 2a shows the measured four-probe longitudinal resistance R_{xx} as a function of charge carrier density $n = (C_{TG}V_{TG} + C_{BG}V_{BG})/e + n_0$ and displacement field (positive direction defined as bottom to top) $D = (-C_{TG}V_{TG} + C_{BG}V_{BG})/2 + D_0$, where C_{TG}, C_{BG} are the top, back gate geometric capacitances; n_0, D_0 are finite offsets (see Supporting Information-1 for details). Figure 2b shows a zoomed-in measurement of R_{xx} as function of n and D, with its Chern number configuration and intra- and interlayer QH transitions marked by the stability diagram (Figure 2c) of layer-polarized QH states. For the ease of the discussion, the same carrier density span of Figures 2b, c is also converted to the overall Landau level (LL) filling factors $\nu = nh/(eB)$ on Fig. 2b top axis, in which n is the corresponding carrier density, ε_0 is the vacuum permittivity, h is Planck's constant, and e is the elementary charge. In our device, the LLs in each graphene layer have a standard fourfold degeneracy, with layer-specific Chern number (number of filled N-type Landau levels in each layer) labeled (three consecutive integers in convention of $N_T|N_M|N_B$ for the top/middle/bottom layer) in each Landau gap(Fig. 2d-m), and total Chern number $N_{tot} = N_T + N_M + N_B$ is labeled on the Fig. 2c bottom axis.

To understand the stability diagram and how charge carriers are added and distributed across each individual layer as a function of n and D, the layer specific LLs are illustrated in Figures 2d-m for typical interlayer transitions (blue shape) and triple-points (red shape) in Figs. 2b, c. For the ease of discussion, we are using a simplified picture where the Landau level broadening is neglected (see Supporting Information-6 for details), so that we can introduce the core qualitative features of the stability dia-

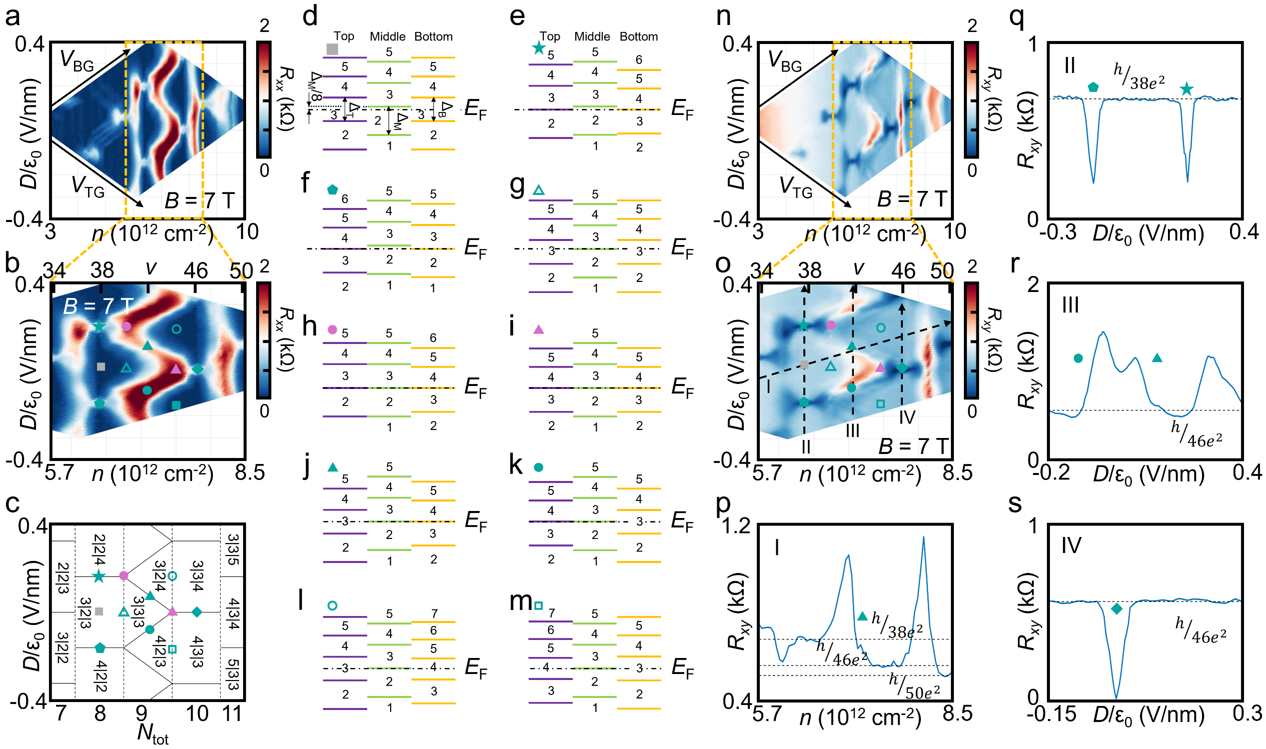

Figure 2. Stability diagram of balanced tTLG quantum Hall states. (a) Longitudinal resistance, R_{xx}, at changing top (V_{TG}) and back gate (V_{BG}) voltages controlling D and n. (b) R_{xx} in the highlighted D-n area from (a). (c) Stability diagram of the layer-polarized quantum Hall states with the Chern numbers $N_T|N_M|N_B$ of the filled fourfold degenerate Landau levels in the top|middle|bottom graphene, and the total LL Chern number N_{tot}. The lines highlight transitions between different layer-polarized QH states involving (dashed) and without changing (solid) N_{tot}. (d)-(m) Energy diagrams of LLs alignment in each layer (with the color matching the layers in Fig. 1a) with respect to the Fermi energy, E_F, at certain QH transitions as marked in (b) and (c). Each layer-specific Landau gap is labeled with the corresponding layer Chern number. (n), (o) Hall resistance, R_{xy}, as a function of D and n in the same range as in (a), (b). (p)-(s) R_{xy} linecuts from (o) labeled by the Roman numerals. R_{xy} exhibits a plateau for each layer-polarized QH state with a height (highlighted by the dashed lines) consistent with the total LL filling ν. At interlayer transitions, R_{xy} behaves non-monotonically possibly due to strong Coulomb coupling and/or Coulomb drag between layers with partially filled LLs.

gram, and leave the discussion on the microscopic details of the extended states versus localized states in disorder-broadened LLs to later part of the manuscript when their consequence on transport becomes more relevant. In this simple picture, increasing n will uniformly move the Landau levels in the top/middle/bottom graphene (marked by the purple/green/yellow lines in Figs. 2d-m), by uniformly increasing the carrier density in each layer. Increasing D will increase (decrease) carrier density in the bottom (top) graphene layer while keeping the overall carrier density constant, and thus moving the LLs in the bottom (top) layer down (up) with respect to the Fermi energy.

We first examine a typical configuration at the center of the 3|2|3| domain, the measured R_{xx} is zero due to only ballistic edge states conducting in each layer. In the simplified picture, the Fermi level lies in the middle of the $N_T = N_B = 3$ Landau gaps (referred as Δ_T, Δ_B) in both the top and bottom layer, and lies in the $N_M = 2$ Landau gap (defined as Δ_M) of the middle layer, $\Delta_M/8$ below the 3rd LL and $7\Delta_M/8$ above the 2nd LL (grey square, Fig. 2d). More accurately, this corresponds to the exact integer filling of $N_T = N_B = 3$ in the top and bottom layer, and filling the 3rd LL in the middle layer by a 3/8 of its density of states (nearly half-filled). Increasing D to lower the LLs in the bottom layer and raising the LLs in the top layer by an equal amount of $\Delta_T/2 = \Delta_B/2$(while keeping the LLs in the middle layer intact) will bring the system to a local high resistance peak corresponding to an interlayer Chern transition (blue star) between the 2|2|4 and 3|2|3 Chern number configurations (hereby denoted as 2|2|4 ⇔ 3|2|3 transition), where corresponding LLs in both top and bottom layers are half-filled (Fig. 2e) and aligned with the Fermi energy, resulting in dissipative bulk conduction, and mark the horizontal (parallel to the n axis) boundary between the two QH domains in the stability diagram. Similarly, decreasing D to raise the LLs in the bottom layer and lower the LLs in the top layer by an equal amount of half filling will bring the system to the interlayer Chern transition of 4|2|2 ⇔ 3|2|3 at the horizontal boundary between their QH domains (Fig. 2f, blue pentagon).

Starting from the center of 3|2|3, increasing n while keeping $D = 0$ will move the LLs in all three layers down in energy (with respect to E_F) by an equal amount. Being closer in energy to the next unfilled LL in the middle layer, the Fermi level first aligns to the 3rd LL in the center layer (half-filled) while still being in the $N_T = N_B = 3$ Landau gaps of the top and the bottom layer (Figure 2g), at the boundary between the 3|2|3 and 3|3|3 Chern number configurations. The measured R_{xx} is surprisingly zero (blue hollow triangle in Fig. 2b) at this intralayer Chern transition, which may be attributed to only the middle layer becoming dissipative while the other two layers are ballistic, in contrast to two dissipative layers at the interlayer Chern number transitions. The common corner of the vertical intralayer Chern transition of 3|2|3 ⇔ 3|3|3 and the horizontal interlayer Chern transition of 2|2|4 ⇔ 3|2|3 marks the triple point (red circle, Fig 2h) where all three layers have the LLs half-filled and dissipative, leading to a local maximum of measured R_{xx}.

The $N_{tot} = 8$ domains are rectangular, similar to the that observed in decoupled twisted bilayers.[29–39] In contrast, the 3|3|3 domain has a triangular shape unique to tTLG. In addition to the vertical boundary from the intralayer transition, the other two boundaries correspond to interlayer Chern transitions of 3|2|4 ⇔ 3|3|3 and 4|2|3 ⇔ 3|3|3 (blue triangle and circle, Figs. 2j, k) between adjacent graphene layers. As a function of n versus D, the carrier density of the top and bottom layer can be tuned by increasing n (new charges added to all three layers of the tTLG system) and by increasing D (redistributing charges from the top layer to the bottom layer), while carrier density in the center layer is independent of D and can only be tuned by the overall carrier density n. As a result of this difference, the interlayer transitions between adjacent layers are slanted, while the interlayer transitions involving the top and bottom layer are still horizontal. Along the boundary of the 3|2|4 ⇔ 3|3|3 transition, as n increases, the D field needed to keep the LLs in both middle and bottom layers aligned with E_F (half-filled) decreases, thus the negative slope. Same for the positive slope along 4|2|3 ⇔ 3|3|3 interlayer transition.

Further increasing n to $N_{tot} = 10$, the domain shape will become rectangular again, whose boundary is marked by the intralayer transition of 3|2|4 ⇔ 3|3|4 and 4|2|3 ⇔ 4|3|3 (hollow blue circle and square, Fig. 2l, m) and interlayer transition of 3|3|4 ⇔ 4|3|3 between the top and bottom layers, consistent with previous observations on different types of intra and interlayer transitions.

Figure 2n shows the measured four-probe transverse resistance R_{xy} as a function of n and D, with the same scan range as in Figure 2a. Figure 2o shows a zoomed-in measurement of R_{xy}, with the same scan range of Figure 2b and thus also marked by Figure 2c. A 1D cut (Figure 2p, along the dashed line I in Fig. 2o) crossing multiple quantized conductance plateau confirms the expected filling factors. The R_{xy} as a function of D (Fig. 2q) across the three $N_{tot} = 8$ domains (along the interpolated dashed line II in Fig. 2o) shows each domain having conductance quantized at the expected value of $G = 4(3/2 + N_{tot}e^2/h) = 38e^2/h$, confirming the total Chern number of $N_{tot} = 8$. The Hall resistance at the interlayer Chern transitions located at the domain boundaries are measured to be smaller than $1/(38e^2/h)$. Similar R_{xy} behavior is observed for the $N_{tot} = 10$ domains (Fig. 2s, along the interpolated dashed line IV in Fig. 2o), but with R_{xy} all the way reaching zero at the 3|3|4 ⇔ 4|3|3 interlayer transition. This unusual behavior is not expected from the individual contributions from each decoupled layer to the overall R_{xy}. The suppression of R_{xy} is observed only at the interlayer transition between the top and bottom layers, and not for interlayer transitions between adjacent layers (Fig. 2r, along the interpolated dashed line III in Fig. 2o). This suggests the underlying mechanism for this exotic behavior may be associated with a strong Coulomb coupling and drag between the top and bottom layers with partially filled LLs and $R_{xy} = 0$ implying possible emergence of exciton condensates. Future Coulomb drag experiments with individual contacts to the top and bottom layers are needed to assertively confirm the exact mechanism and investigate its dependence on n and D.

Due to the system's mirror symmetry against the center layer, domains centered around the $D = 0$ axis have an equal top and bottom Chern number. At the center of these domains, the top and bottom layers are exactly integer-filled, corresponding to E_F in the center of the LL gap. However, depending on the magnetic field B, filling for middle layer LLs at the domain center can be arbitrary, leading to distinct features of the resulting stability diagram.

General Stability Diagram. Figure 3a shows the measured four-probe longitudinal resistance R_{xx} at B =5 T, with Figure 3b showing a zoomed-in scan and the corresponding stability diagram (Figure 3c, with zooming in around 5|4|5 shown in Figure 3g). At the center of the 5|3|5 domain (grey square, Figure 3d), the Fermi level lies in the middle of the $N_T = N_B = 5$ Landau gaps ($\Delta_T = \Delta_B$) in both the top and bottom layers, similar to the previous stability diagram. In contrast, the $N_M = 4$ LL is now 1/8 filled instead of 3/8 filled, corresponding to the Fermi level $3\Delta_M/8$ below the 4th LL and $5\Delta_M/8$ above the 3rd LL in the middle layer.

As a result, at the center of the 5|3|5 domain, the 4th LL in the center layer is only slightly closer (by 1/8 of the corresponding gap) to the Fermi level than the 6th LLs in top and bottom layer. Increasing carrier density n at D = 0 will bring the N_M = 4 LL in the middle layer to the Fermi level (blue triangle, Figure 3h), corresponding to the 5|3|5 ⇔ 5|4|5 intra-middle-layer transition, similar to the previous stability diagram.

In contrast to the previous stability diagram where the LL in the middle layer is significantly closer to E_F, the smaller advantage of middle layer here can be easily overtaken by the top (bottom) layer with a negative (positive) D field, that brings the next unfilled LL in the top (bottom) layer closer to E_F than that in center layer, marked by a grey pentagon (star) and depicted by Figure 3e(f). Increasing the carrier density from here at negative (positive) D field will therefore bring the LL in the top (bottom) layer to E_F first, corresponding to the intralayer transition 5|3|5⇔ 6|3|5 (5|3|5⇔ 5|3|6) of the top (bottom) layer instead.

The size of the triangular domain 5|4|5 is proportional to the D span of the 5|3|5⇔ 5|4|5 intra-middle-layer transition, which is now significantly reduced compared to the previous stability diagram (Fig. 2). With finite broadening (see Supporting Information-6 for details) of the local high R_{xx} resistance peaks from the top and bottom intralayer transitions, non-zero R_{xx} resistances are observed at the entire span of the triangular 5|4|5 domain. Similar (and smaller) triangular domains can also be found along N_{tot} = 12.5 and N_{tot} = 15.5.

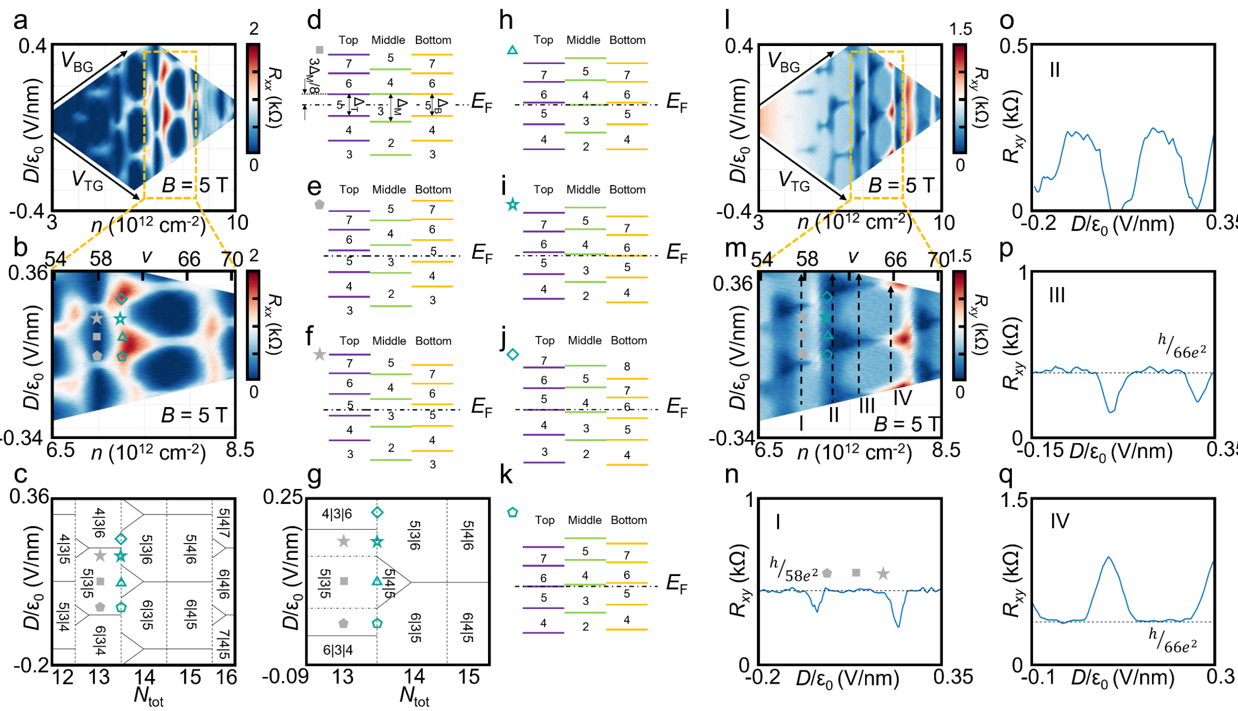

Figure 3. General stability diagram of tTLG quantum Hall states. (a) R_{xx} as a function D and n tuned by the top (V_{TG}) and back gate (V_{BG}) voltages. (b) Zoomed-in scan of the yellow area from (a) with resistance peaks corresponding to transitions between different layer-polarized QH configurations where the top axis labels the total LL filling factor ν. (c) General stability diagram of layer-polarized quantum Hall states in the top|middle|bottom layer with the corresponding Chern numbers $N_T|N_M|N_B$ where the total Chern number is N_{tot}. The dashed (solid) lines trace transitions between layer-polarized QH states with (without) changing N_{tot}. (d)-(f) LLs alignment controlled by D at a constant n within the 5|3|5 layer-polarized QH state. The numbers label the layer Chern number of the Landau gap of the corresponding graphene. (g) A zoomed-in layer-polarized QH state stability diagram from (c). The markers indicate the position of the selected QH transitions on the n-D map (b) and diagrams (c), (g). (h)-(k) LL alignment at selected transitions between the N_{tot} = 13 and N_{tot} = 14 QH states. (l), (m) R_{xy} in the same range of D and n as in (a), (b). (n)-(q) Interpolated R_{xy} linecuts [indicated in (m) and labeled by the Roman numerals] showing the R_{xy} dips at interlayer transitions between layer-specific QH states.

Next to these smaller triangular domains, larger trapezoid domains (such as 5|3|6 and 6|3|5|) with the measured zero R_{xx} can be found, as expected from all three layers entering ballistic QH edge transport. Further increasing carrier density will trigger an intra-middle-layer transition (i.e., 5|3|6 ⇔ 5|4|6) with R_{xx} = 0, similar to the previous case, together making a large combined R_{xx} = 0 region.

Figure 3l (Figure 3m) shows the measured four-probe transverse resistance R_{xy} as a function of n and D, with the same scan range as figure 3a (Figure 3b). Figures 3n-q show a few signature interpolated 1D cuts along the dashed lines I – IV labeled in Figure 3m, respectively. The dips in R_{xy} previously observed at the top-bottom interlayer transitions are now observed for the entire span of the smaller triangle domains. At the boundary of the small triangular domain 5|4|5, the finite broadening of the top-middle transition 5|4|5 ⇔ 5|3|6 and 5|4|5 ⇔ 6|3|5 into the center of the 5|4|5 domain allows indirect top-bottom transition of 5|3|6 ⇔ 5|4|5 ⇔ 6|3|5 within the 5|4|5 domain, consistent with R_{xy} dips possibly arising from strong Coulomb drag between partially-filled top and bottom layers and emergence of exciton condensates. For the larger trapezoid domains with R_{xx} = 0, their R_{xy} is consistent with the quantized conductance expected from the corresponding N_{tot}.

CONCLUSIONS

In conclusion, we report layer-polarized quantum Hall states of a consecutively twisted tTLG device, and map out the QH stability diagram of tTLG, systematically identifying layer-specific Chern numbers, triple points, intra- and interlayer Chern transitions as a function of local gate voltages, carrier density and displacement field. We show that the interplay between QH states in the tTLG QH stability diagram is significantly more diverse in mechanism and richer in transport behaviors, compared to that of the previously studied bilayer systems. The stability diagram systematically characterizes interlayer screening, layer-polarization and interlayer carrier redistribution, providing quantitative experimental guidance and reference for electrostatically tuning of the tTLG platform. We show that the shape of the stability diagram, as well as its transport signatures, can be sensitively tuned by changing relative LL alignment across the three layers. When the top and bottom layers both have partially filled LLs at the direct interlayer transition (line-shaped) or indirect interlayer transition (triangular-shaped), we report unusual transport signatures of R_{xy} = 0, that can potentially be attributed to emergence of exciton condensates due to strong interlayer Coulomb coupling. This work paves a path towards future study of layer-polarized electronics states in tTLG, and how the rich interactions and reconstructions between them can lead novel correlated and exotic quantum phenomena.

METHODS

The twisted trilayer graphene (tTLG) stack was made by utilizing the "cut and stack" method.[40] A suitable monolayer graphene (MLG) was first characterized using optical microscopy. The MLG flake was then cut with the cantilever of an atomic force microscope (AFM, from Park Systems: model XE7) into three separate pieces. To make a tTLG stack, a poly (bisphenol A carbonate) (PC) and polydimethylsiloxane (PDMS) stamp attached to a glass slide was used to pick up a top hexagonal boron nitride (hBN) flake.[41] After that, a few-layer graphite flake (working as a top gate) was picked up followed by a middle hBN to electrically and physically isolate the top gate. The three precut MLG flakes were then sequentially picked up. After each pick up of a precut MLG piece, the rotation stage with the remaining graphene was consecutively twisted by ~ 2°. Following this, a bottom hBN flake was picked up to encapsulate the tTLG. The assembled stack was released onto a SiO_2(285 nm)/Si substrate at 180°C. Upon cooling down to room temperature, the substrate with the stack was successively rinsed in chloroform, acetone and isopropanol to clean the remains of PC. Next, by using the AFM, bubble-free areas of tTLG were identified to ensure the absence of strain and/or defects that could potentially reduce the device quality and compromise electrical transport. Then, Ohmic edge contacts[42] to graphene were fabricated via electron-beam lithography followed by reactive-ion etching and electron-beam evaporation of metal (Cr/Pd/Au, with thicknesses of 1 nm /5 nm/>180 nm). Finally, the tTLG region was shaped into a multiterminal device (Fig. 1b) during an additional round of electron-beam lithography and subsequent reactive-ion etching.

The electrical and magneto-transport data was taken while the device was measured in a four-probe configuration under a 10 nA current bias (with an AC frequency of 17.777 Hz) inside a Bluefors LD250 cryostat at a temperature of T = 20 mK. In all regions of the device, contact 1 was used as a source of the driven current, and contacts 6 were used as a drain. The longitudinal, R_{xx}, (transverse, R_{xy}) resistances discussed in the main manuscript are found from the voltage measured between contact 9 and contact 8 (contact 9 and contact 3) shown in Figure 1b. To drive the current and measure voltages between different contacts, lock-in amplifiers (Stanford Research Systems: model GS200) were used. The graphite top gate and Si back gate voltages were controlled by two DC voltage sources (Yokogawa: Model GS200 and Keithley Instruments: Model 2400 respectively).

The studied device has a shape (Fig. 1b) distinct from a perfect Hall bar geometry, thus the measured resistance under applied magnetic field is always a linear combination of longitudinal (along the driven current) and Hall resistance. To account for this, the longitudinal resistance [symmetric as $R_{xx}(B)$] is extracted from the measured resistance between two given contacts $R_{\text{measured}}(B)$] according $R_{xx}(B) = [R_{\text{measured}}(B) + R_{\text{measured}}(-B)]/2$. Similarly, the anti-symmetric, as a function of magnetic field, transverse Hall resistance is found $R_{xy}(B) = [R_{\text{measured}}(B) - R_{\text{measured}}(-B)]/2$, where $B \geq 0$.

ASSOCIATED CONTENT

Supporting Information. Calculation of total charge carrier density and displacement field from gate capacitive coupling; data from additional region of measured device; characterization of two moiré periodicities; electrostatic simulation of layer Landau level fillings; characterization of electrostatic screening by constituent graphene layers; effect of disorder on Landau level broadening; electric field screening by partially filled Landau levels. This material is available free of charge via the Internet at http://pubs.acs.org.

AUTHOR INFORMATION

Corresponding Author

*Ke Wang – School of Physics and Astronomy, University of Minnesota, Minneapolis, Minnesota 55455, USA;
Email: kewang@umn.edu.

Present Addresses

†Konstantin Davydov – Department of Materials Science and Engineering, University of Maryland, College Park, Maryland 20742, USA.

Author Contributions

K.D. fabricated the device and performed the electrical transport measurements, under the supervision of K.Wan. K.D. analyzed the experimental data with input from D.L. and J.A.T., under the supervision of K.Wan. K.Wat. and T.T. provided the BN crystals. K.D. and K.Wan. wrote the manuscript with input from D.L. and J.A.T. K.Wan. conceived the experiment. All authors have given approval to the final version of the manuscript.

Funding Sources

This work was supported by NSF DMREF Award 1922165. K.Wat. and T.T. acknowledge support from the JSPS KAKENHI (Grant Numbers 20H00354, 21H05233 and 23H02052) and World Premier International Research Center Initiative (WPI), MEXT, Japan.

ACKNOWLEDGMENT

We thank B. Shklovskii and H. Goldman for helpful discussions. This work was supported by NSF DMREF Award 1922165. Portions of this work were conducted in the Minnesota Nano Center, which is supported by the National Science Foundation through the National Nanotechnology Coordinated Infrastructure (NNCI) under Award Number ECCS-2025124. Portions of the hexagonal boron nitride material used in this work were provided by K.Wat. and T. T. K.Wat. and T.T. acknowledge support from the JSPS KAKENHI (Grant Numbers 20H00354, 21H05233 and 23H02052) and World Premier International Research Center Initiative (WPI), MEXT, Japan.

ABBREVIATIONS

AFM, atomic force microscope; hBN, hexagonal boron nitride; LL, Landau level; MLG, monolayer graphene; MoM, moiré-of-moiré; PC, poly (bisphenol A carbonate); PDMS, polydimethylsiloxane; QH, quantum Hall; SdH, Shubnikov-de Haas; tQD, triple quantum dot; tTLG, twisted trilayer graphene.

REFERENCES

(1) Cao, Y.; Fatemi, V.; Fang, S.; Watanabe, K.; Taniguchi, T.; Kaxiras, E.; Jarillo-Herrero, P. Unconventional Superconductivity in Magic-Angle Graphene Superlattices. *Nature* **2018**, *556* (7699), 43–50. https://doi.org/10.1038/nature26160.

(2) Yankowitz, M.; Chen, S.; Polshyn, H.; Zhang, Y.; Watanabe, K.; Taniguchi, T.; Graf, D.; Young, A. F.; Dean, C. R. Tuning Superconductivity in Twisted Bilayer Graphene. *Science* **2019**, *363* (6431), 1059–1064. https://doi.org/10.1126/science.aav1910.

(3) Sharpe, A. L.; Fox, E. J.; Barnard, A. W.; Finney, J.; Watanabe, K.; Taniguchi, T.; Kastner, M. A.; Goldhaber-Gordon, D. Emergent Ferromagnetism near Three-Quarters Filling in Twisted Bilayer Graphene. *Science* **2019**, *365* (6453), 605–608. https://doi.org/10.1126/science.aaw3780.

(4) Cao, Y.; Fatemi, V.; Demir, A.; Fang, S.; Tomarken, S. L.; Luo, J. Y.; Sanchez-Yamagishi, J. D.; Watanabe, K.; Taniguchi, T.; Kaxiras, E.; Ashoori, R. C.; Jarillo-Herrero, P. Correlated Insulator Behaviour at Half-Filling in Magic-Angle Graphene Superlattices. *Nature* **2018**, *556* (7699), 80–84. https://doi.org/10.1038/nature26154.

(5) Nuckolls, K. P.; Oh, M.; Wong, D.; Lian, B.; Watanabe, K.; Taniguchi, T.; Bernevig, B. A.; Yazdani, A. Strongly Correlated Chern Insulators in Magic-Angle Twisted Bilayer Graphene. *Nature* **2020**, *588* (7839), 610–615. https://doi.org/10.1038/s41586-020-3028-8.

(6) Wu, S.; Zhang, Z.; Watanabe, K.; Taniguchi, T.; Andrei, E. Y. Chern Insulators, van Hove Singularities and Topological Flat Bands in Magic-Angle Twisted Bilayer Graphene. *Nat. Mater.* **2021**, *20* (4), 488–494. https://doi.org/10.1038/s41563-020-00911-2.

(7) Serlin, M.; Tschirhart, C. L.; Polshyn, H.; Zhang, Y.; Zhu, J.; Watanabe, K.; Taniguchi, T.; Balents, L.; Young, A. F. Intrinsic Quantized Anomalous Hall Effect in a Moiré Heterostructure. *Science* **2020**, *367* (6480), 900–903. https://doi.org/10.1126/science.aay5533.

(8) Cai, J.; Anderson, E.; Wang, C.; Zhang, X.; Liu, X.; Holtzmann, W.; Zhang, Y.; Fan, F.; Taniguchi, T.; Watanabe, K.; Ran, Y.; Cao, T.; Fu, L.; Xiao, D.; Yao, W.; Xu, X. Signatures of Fractional Quantum Anomalous Hall States in Twisted MoTe2. *Nature* **2023**, *622* (7981), 63–68. https://doi.org/10.1038/s41586-023-06289-w.

(9) Park, H.; Cai, J.; Anderson, E.; Zhang, Y.; Zhu, J.; Liu, X.; Wang, C.; Holtzmann, W.; Hu, C.; Liu, Z.; Taniguchi, T.; Watanabe, K.; Chu, J.-H.; Cao, T.; Fu, L.; Yao, W.; Chang, C.-Z.; Cobden, D.; Xiao, D.; Xu, X. Observation of Fractionally Quantized Anomalous Hall Effect. *Nature* **2023**, *622* (7981), 74–79. https://doi.org/10.1038/s41586-023-06536-0.

(10) Xu, F.; Sun, Z.; Jia, T.; Liu, C.; Xu, C.; Li, C.; Gu, Y.; Watanabe, K.; Taniguchi, T.; Tong, B.; Jia, J.; Shi, Z.; Jiang, S.; Zhang, Y.; Liu, X.; Li, T. Observation of Integer and Fractional Quantum Anomalous Hall Effects in Twisted Bilayer MoTe 2. *Phys. Rev. X* **2023**, *13* (3), 031037. https://doi.org/10.1103/PhysRevX.13.031037.

(11) Reddy, A. P.; Alsallom, F.; Zhang, Y.; Devakul, T.; Fu, L. Fractional Quantum Anomalous Hall States in Twisted Bilayer MoTe 2 and WSe 2. *Phys. Rev. B* **2023**, *108* (8), 085117. https://doi.org/10.1103/PhysRevB.108.085117.

(12) Xia, Y.; Han, Z.; Watanabe, K.; Taniguchi, T.; Shan, J.; Mak, K. F. Superconductivity in Twisted Bilayer WSe2. *Nature* **2025**, *637* (8047), 833–838. https://doi.org/10.1038/s41586-024-08116-2.

(13) Guo, Y.; Pack, J.; Swann, J.; Holtzman, L.; Cothrine, M.; Watanabe, K.; Taniguchi, T.; Mandrus, D. G.; Barmak, K.; Hone, J.; Millis, A. J.; Pasupathy, A.; Dean, C. R. Superconductivity in 5.0° Twisted Bilayer WSe2. *Nature* **2025**, *637* (8047), 839–845. https://doi.org/10.1038/s41586-024-08381-1.

(14) Kang, K.; Shen, B.; Qiu, Y.; Zeng, Y.; Xia, Z.; Watanabe, K.; Taniguchi, T.; Shan, J.; Mak, K. F. Evidence of the Fractional Quantum Spin Hall Effect in Moiré MoTe2. *Nature* **2024**, *628* (8008), 522–526. https://doi.org/10.1038/s41586-024-07214-5.

(15) Park, J. M.; Cao, Y.; Watanabe, K.; Taniguchi, T.; Jarillo-Herrero, P. Tunable Strongly Coupled Superconductivity in Magic-Angle Twisted Trilayer Graphene. *Nature* **2021**, *590*

(7845), 249–255. https://doi.org/10.1038/s41586-021-03192-0.
(16) Hao, Z.; Zimmerman, A. M.; Ledwith, P.; Khalaf, E.; Najafabadi, D. H.; Watanabe, K.; Taniguchi, T.; Vishwanath, A.; Kim, P. Electric Field–Tunable Superconductivity in Alternating-Twist Magic-Angle Trilayer Graphene. *Science* **2021**, *371* (6534), 1133–1138. https://doi.org/10.1126/science.abg0399.
(17) Zhang, X.; Tsai, K.-T.; Zhu, Z.; Ren, W.; Luo, Y.; Carr, S.; Luskin, M.; Kaxiras, E.; Wang, K. Correlated Insulating States and Transport Signature of Superconductivity in Twisted Trilayer Graphene Superlattices. *Phys. Rev. Lett.* **2021**, *127* (16), 166802. https://doi.org/10.1103/PhysRevLett.127.166802.
(18) Uri, A.; de la Barrera, S. C.; Randeria, M. T.; Rodan-Legrain, D.; Devakul, T.; Crowley, P. J. D.; Paul, N.; Watanabe, K.; Taniguchi, T.; Lifshitz, R.; Fu, L.; Ashoori, R. C.; Jarillo-Herrero, P. Superconductivity and Strong Interactions in a Tunable Moiré Quasicrystal. *Nature* **2023**, *620* (7975), 762–767. https://doi.org/10.1038/s41586-023-06294-z.
(19) Hoke, J. C.; Li, Y.; Hu, Y.; May-Mann, J.; Watanabe, K.; Taniguchi, T.; Devakul, T.; Feldman, B. E. Imaging Supermoire Relaxation and Conductive Domain Walls in Helical Trilayer Graphene. arXiv October 21, 2024. https://doi.org/10.48550/arXiv.2410.16269.
(20) Zhu, Z.; Carr, S.; Massatt, D.; Luskin, M.; Kaxiras, E. Twisted Trilayer Graphene: A Precisely Tunable Platform for Correlated Electrons. *Phys. Rev. Lett.* **2020**, *125* (11), 116404. https://doi.org/10.1103/PhysRevLett.125.116404.
(21) Zhang, Y.; Polski, R.; Lewandowski, C.; Thomson, A.; Peng, Y.; Choi, Y.; Kim, H.; Watanabe, K.; Taniguchi, T.; Alicea, J.; von Oppen, F.; Refael, G.; Nadj-Perge, S. Promotion of Superconductivity in Magic-Angle Graphene Multilayers. *Science* **2022**, *377* (6614), 1538–1543. https://doi.org/10.1126/science.abn8585.
(22) Ren, W.; Davydov, K.; Zhu, Z.; Ma, J.; Watanabe, K.; Taniguchi, T.; Kaxiras, E.; Luskin, M.; Wang, K. Tunable Inter-Moiré Physics in Consecutively Twisted Trilayer Graphene. *Phys. Rev. B* **2024**, *110* (11), 115404. https://doi.org/10.1103/PhysRevB.110.115404.
(23) Xia, L.-Q.; de la Barrera, S. C.; Uri, A.; Sharpe, A.; Kwan, Y. H.; Zhu, Z.; Watanabe, K.; Taniguchi, T.; Goldhaber-Gordon, D.; Fu, L.; Devakul, T.; Jarillo-Herrero, P. Topological Bands and Correlated States in Helical Trilayer Graphene. *Nat. Phys.* **2025**, *21* (2), 239–244. https://doi.org/10.1038/s41567-024-02731-6.
(24) Eng, K.; Ladd, T. D.; Smith, A.; Borselli, M. G.; Kiselev, A. A.; Fong, B. H.; Holabird, K. S.; Hazard, T. M.; Huang, B.; Deelman, P. W.; Milosavljevic, I.; Schmitz, A. E.; Ross, R. S.; Gyure, M. F.; Hunter, A. T. Isotopically Enhanced Triple-Quantum-Dot Qubit. *Science Advances* **2015**, *1* (4), e1500214. https://doi.org/10.1126/sciadv.1500214.
(25) Gaudreau, L.; Granger, G.; Kam, A.; Aers, G. C.; Studenikin, S. A.; Zawadzki, P.; Pioro-Ladrière, M.; Wasilewski, Z. R.; Sachrajda, A. S. Coherent Control of Three-Spin States in a Triple Quantum Dot. *Nature Phys* **2012**, *8* (1), 54–58. https://doi.org/10.1038/nphys2149.
(26) Kratochwil, B.; Koski, J. V.; Landig, A. J.; Scarlino, P.; Abadillo-Uriel, J. C.; Reichl, C.; Coppersmith, S. N.; Wegscheider, W.; Friesen, M.; Wallraff, A.; Ihn, T.; Ensslin, K. Charge Qubit in a Triple Quantum Dot with Tunable Coherence. *Phys. Rev. Res.* **2021**, *3* (1), 013171. https://doi.org/10.1103/PhysRevResearch.3.013171.
(27) Blumoff, J. Z.; Pan, A. S.; Keating, T. E.; Andrews, R. W.; Barnes, D. W.; Brecht, T. L.; Croke, E. T.; Euliss, L. E.; Fast, J. A.; Jackson, C. A. C.; Jones, A. M.; Kerckhoff, J.; Lanza, R. K.; Raach, K.; Thomas, B. J.; Velunta, R.; Weinstein, A. J.; Ladd, T. D.; Eng, K.; Borselli, M. G.; Hunter, A. T.; Rakher, M. T. Fast and High-Fidelity State Preparation and Measurement in Triple-Quantum-Dot Spin Qubits. *PRX Quantum* **2022**, *3* (1), 010352. https://doi.org/10.1103/PRXQuantum.3.010352.
(28) Klitzing, K. v.; Dorda, G.; Pepper, M. New Method for High-Accuracy Determination of the Fine-Structure Constant Based on Quantized Hall Resistance. *Phys. Rev. Lett.* **1980**, *45* (6), 494–497. https://doi.org/10.1103/PhysRevLett.45.494.
(29) Sanchez-Yamagishi, J. D.; Taychatanapat, T.; Watanabe, K.; Taniguchi, T.; Yacoby, A.; Jarillo-Herrero, P. Quantum Hall Effect, Screening, and Layer-Polarized Insulating States in Twisted Bilayer Graphene. *Phys. Rev. Lett.* **2012**, *108* (7), 076601. https://doi.org/10.1103/PhysRevLett.108.076601.
(30) Sanchez-Yamagishi, J. D.; Luo, J. Y.; Young, A. F.; Hunt, B. M.; Watanabe, K.; Taniguchi, T.; Ashoori, R. C.; Jarillo-Herrero, P. Helical Edge States and Fractional Quantum Hall Effect in a Graphene Electron–Hole Bilayer. *Nature Nanotech* **2017**, *12* (2), 118–122. https://doi.org/10.1038/nnano.2016.214.
(31) Li, Q.; Chen, Y.; Wei, L.; Chen, H.; Huang, Y.; Zhu, Y.; Zhu, W.; An, D.; Song, J.; Gan, Q.; Zhang, Q.; Watanabe, K.; Taniguchi, T.; Shi, X.; Novoselov, K. S.; Wang, R.; Yu, G.; Wang, L. Strongly Coupled Magneto-Exciton Condensates in Large-Angle Twisted Double Bilayer Graphene. *Nat Commun* **2024**, *15* (1), 5065. https://doi.org/10.1038/s41467-024-49406-7.
(32) Kim, D.; Kang, B.; Choi, Y.-B.; Watanabe, K.; Taniguchi, T.; Lee, G.-H.; Cho, G. Y.; Kim, Y. Robust Interlayer-Coherent Quantum Hall States in Twisted Bilayer Graphene. *Nano Lett.* **2023**, *23* (1), 163–169. https://doi.org/10.1021/acs.nanolett.2c03836.
(33) Kim, Y.; Moon, P.; Watanabe, K.; Taniguchi, T.; Smet, J. H. Odd Integer Quantum Hall States with Interlayer Coherence in Twisted Bilayer Graphene. *Nano Lett.* **2021**, *21* (10), 4249–4254. https://doi.org/10.1021/acs.nanolett.1c00360.
(34) Dong, B.; Zhao, K.; Watanabe, K.; Taniguchi, T.; Lu, J.; Zhao, J.; Wu, F.; Zhang, J.; Han, Z. Quantized Landau-Level Crossing Checkerboard in Large-Angle Twisted Graphene. arXiv December 4, 2024. https://doi.org/10.48550/arXiv.2412.03004.
(35) Kim, S.; Kim, D.; Watanabe, K.; Taniguchi, T.; Smet, J. H.; Kim, Y. Orbitally Controlled Quantum Hall States in Decoupled Two-Bilayer Graphene Sheets. *Advanced Science* **2023**, *10* (23), 2300574. https://doi.org/10.1002/advs.202300574.
(36) Rickhaus, P.; de Vries, F. K.; Zhu, J.; Portoles, E.; Zheng, G.; Masseroni, M.; Kurzmann, A.; Taniguchi, T.; Watanabe, K.; MacDonald, A. H.; Ihn, T.; Ensslin, K. Correlated Electron-Hole State in Twisted Double-Bilayer Graphene. *Science* **2021**, *373* (6560), 1257–1260. https://doi.org/10.1126/science.abc3534.
(37) de Vries, F. K.; Zhu, J.; Portolés, E.; Zheng, G.; Masseroni, M.; Kurzmann, A.; Taniguchi, T.; Watanabe, K.; MacDonald, A. H.; Ensslin, K.; Ihn, T.; Rickhaus, P. Combined Minivalley and Layer Control in Twisted Double Bilayer Graphene. *Phys. Rev. Lett.* **2020**, *125* (17), 176801. https://doi.org/10.1103/PhysRevLett.125.176801.
(38) Pezzini, S.; Mišeikis, V.; Piccinini, G.; Forti, S.; Pace, S.; Engelke, R.; Rossella, F.; Watanabe, K.; Taniguchi, T.; Kim, P.; Coletti, C. 30°-Twisted Bilayer Graphene Quasicrystals from Chemical Vapor Deposition. *Nano Lett.* **2020**, *20* (5), 3313–3319. https://doi.org/10.1021/acs.nanolett.0c00172.
(39) Yuan, Y.; Liu, L.; Zhu, J.; Dong, J.; Chu, Y.; Wu, F.; Du, L.; Watanabe, K.; Taniguchi, T.; Shi, D.; Zhang, G.; Yang, W. Interplay of Landau Quantization and Interminivalley Scatterings in a Weakly Coupled Moiré Superlattice. *Nano Lett.*

2024, *24* (22), 6722–6729. https://doi.org/10.1021/acs.nanolett.4c01411.

(40) Saito, Y.; Ge, J.; Watanabe, K.; Taniguchi, T.; Young, A. F. Independent Superconductors and Correlated Insulators in Twisted Bilayer Graphene. *Nat. Phys.* **2020**, *16* (9), 926–930. https://doi.org/10.1038/s41567-020-0928-3.

(41) Dean, C. R.; Young, A. F.; Meric, I.; Lee, C.; Wang, L.; Sorgenfrei, S.; Watanabe, K.; Taniguchi, T.; Kim, P.; Shepard, K. L.; Hone, J. Boron Nitride Substrates for High-Quality Graphene Electronics. *Nature Nanotech* **2010**, *5* (10), 722–726. https://doi.org/10.1038/nnano.2010.172.

(42) Wang, L.; Meric, I.; Huang, P. Y.; Gao, Q.; Gao, Y.; Tran, H.; Taniguchi, T.; Watanabe, K.; Campos, L. M.; Muller, D. A.; Guo, J.; Kim, P.; Hone, J.; Shepard, K. L.; Dean, C. R. One-Dimensional Electrical Contact to a Two-Dimensional Material. *Science* **2013**, *342* (6158), 614–617. https://doi.org/10.1126/science.1244358.

.

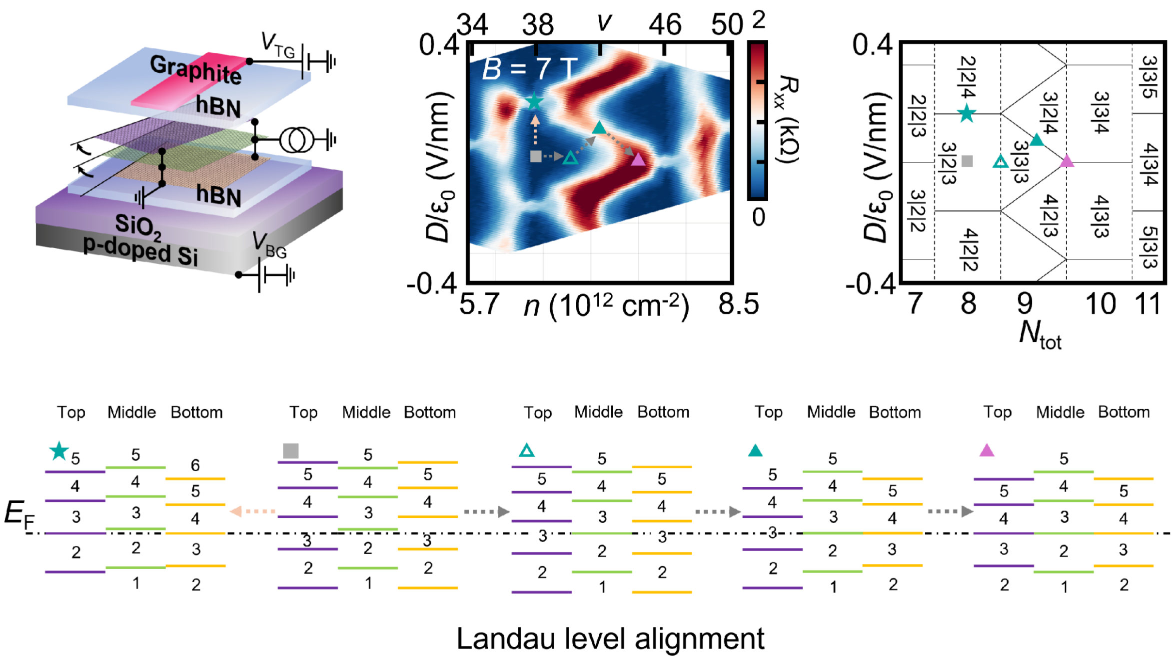

For Table of Contents Only.